Journal of Materials Science: Materials in Electronics
https://doi.org/10.1007/s10854-020-03940-4

$Ca_9Gd(PO_4)_7$:Sm^{3+}—a novel single-phased down converting orange-red-emitting nanophosphor

Anju Siwach[1] · Mandeep Dalal[2] · Manju Dahiya[1] · Dinesh Kumar[1]

Received: 3 April 2020 / Accepted: 3 July 2020

Abstract
Nanocrystalline orange-red-emitting white voluminous powdered samples of Sm^{3+}-doped $Ca_9Gd(PO_4)_7$ phosphor (CGPS) were synthesized by highly efficient solution combustion route. Highly advanced characterization techniques like X-ray diffraction (XRD), Transmission electron microscopy (TEM), and Photoluminescence (PL) spectroscopy were used to characterize the series of samples systematically. The structural properties of $Ca_9Gd_{0.88}(PO_4)_7$:$0.12Sm^{3+}$ (best emitting composition) phosphor were examined in detail via Rietveld refinement analysis to get the information about its structural prototype and crystal phase purity. Phase analysis results of the best emitting composition revealed that the introduction of dopant (Sm^{3+}) ion into the host matrix did not induce any modification in the crystal structure and it further confirmed the crystallization of the $Ca_9Gd_{0.88}(PO_4)_7$:$0.12Sm^{3+}$ phosphor in a trigonal lattice with R*3c*(161) space group. With the help of the Scherrer's equation, the average crystallite size of $Ca_9Gd_{0.88}Sm_{0.12}(PO_4)_7$ system was found to be 40–50 nm. The PL investigations resulted that the optimum Sm^{3+} ion concentration in $Ca_9Gd(PO_4)_7$ host matrix was 12 mol%. Diffuse reflectance (DR) measurements gave the band-gap value of 4.16 eV for $Ca_9Gd_{0.88}Sm_{0.12}(PO_4)_7$ nanophosphor. Detailed PL studies of CGPS phosphors indicated that with the excitation wavelength of 403 nm there was an intense orange-red emission appearing at 600 nm due to the partially electric and partially magnetic dipole allowed $^4G_{5/2} \rightarrow {}^6H_{7/2}$ transition. The critical energy transfer distance (R_c) was calculated in accordance with Van Uitert model which came out to be 21 Å and the proposed mechanism behind energy transfer between different Sm^{3+} ions was analyzed to be dipole–quadrupole interactions using Dexter's analysis. In addition to the radiative lifetime (2.4 ms), non-radiative transition rate (142.9 s^{-1}) and the value of quantum efficiency (75%) were also analyzed with the help of Auzel's fit function. The results as-obtained favor the potential utility of these promising nanophosphors in the domain of lighting for white LEDs.

1 Introduction

As of late, solid-state lighting using white light-emitting diodes (WLEDs) have attracted worldwide attention because of their significant benefits over customary light sources including energy saving, safety, dependability, maintenance, and environmentally cordial features. Latterly, the major attention of researchers has been drawn to obtain white light emission, as a result of which, the phosphor-converted white light-emitting diodes are coming out as a vital source of solid-state illumination in the field of lighting and displays [1–8]. Rare-earth ion-doped nano-scaled phosphors are the competent luminescent materials and a significant component of phosphor-converted white LED (pc-WLED). Moreover, it is also well known that reducing the size of synthesized phosphor to the nanoscale can decrease the extent of non-radiative relaxation as well as the extent of internal scattering which ultimately leads to the enhancement of luminescence efficacy [9, 10]. Thus, a large number of nano-scaled phosphors with increased luminescence power have been synthesized so far and still gaining significant attention of researchers as they are used to generate white emission. The formation of effectual, durable, and single-phase white light-emitting phosphors is one of the key strategies, the reason being that they can confront the re-absorption for blue or UV light by the red/green-emitting phosphors and the mixing of RGB phosphors [11, 12]. Accordingly, it can heighten the luminescence efficiency and color reproducibility of the

✉ Dinesh Kumar
dineshdalal8@rediffmail.com

[1] Department of Chemistry, Deenbandhu Chhotu Ram University of Science & Technology, Murthal, Sonepat 131039, India

[2] Department of Chemistry, Maharshi Dayanand University, Rohtak 124001, India

Published online: 18 July 2020

white light source and thus, proving itself a cost-efficient system [13].

The first white LED (WLED) was developed by Nichia Corporation in 1996 by combining a yellow-emitting phosphor of YAG:Ce^{3+} with a blue LED chip which came into play soon at commercial level [14]. Although this kind of WLED was widely in industries, it has some major drawbacks like low color rendering and high color temperature due to the lack of red-emitting component in its emission spectra. To overcome these shortcomings, an ultraviolet (UV) or near-UV LED was developed by combining blue LED chip with tricolor RGB phosphors [3, 15]. Moreover, the Y_2O_2S:Eu^{3+} red-emitting phosphor has been synthesized and commercialized [16], that can readily absorb moisture and require high temperature for its decomposition. However, it results into the evolution of harmful products into the environment. Hence, there is a need to synthesize such novel red or orange-red-emitting phosphors which can simply overcome these drawbacks.

The trivalent rare-earth ions are extensively used in lighting device because doping of such ions produced tremendous emission colors on ultraviolet excitation and thus give rise to prominent luminescence properties. This behavior of lanthanide ions may be attributed to their 4*f*-4*f* intra-configurational and 5*d*-4*f* inter-configurational transitions [11, 17]. Among several rare-earth ions, trivalent Sm^{3+} ions having electronic configuration [Xe]$4f^5 5d^0 6s^0$ are excellent luminescence centers that provide greater radiation stability and high lumen output. This is relevant that both Eu^{3+} ion and Sm^{3+} ion-doped phosphors show red and orange-red emission. However, phosphors doped with Eu^{3+} ions show distinctive photoluminescence only under excitation of near-UV radiation, which confines their usability in synthesizing WLEDs, while Sm^{3+}-doped phosphors are quite easily irradiated by the radiation of blue region [4]. When compared with Eu^{3+}, it is found that Sm^{3+} is an indispensable dopant ion for inorganic host matrix to bring out orange-red emission because of its $^4G_{5/2} \rightarrow {}^6H_J$ (where $J = 5/2, 7/2, 9/2, 11/2$) transitions [4, 18, 19]. The predominate electronic transition of trivalent samarium ion occurring at nearly 600 nm ($^4G_{5/2} \rightarrow {}^6H_{7/2}$) [20] is accountable for its bright orange-red emission and further its applications in fabrication of tricolor phosphor-based pc-WLEDs.

Many inorganic or organic nanophosphors have already been studied to generate white LEDs. Recently, one type among the broad spectrum of nano-materials, $A_9B(PO_4)_7$ inorganic phosphate compounds (where *A* can be Ca^{2+} or Sr^{2+} or Ba^{2+} and *B* can be La^{3+}, Y^{3+}, Gd^{3+} or Bi^{3+}) have attracted the attention of researchers and scientists because of their uncommon luminescence properties. These phosphates have fine chemical stability, good optical band-gap values, and can easily be synthesized by diverse routes like solid-state reaction, hydrothermal, and solution combustion methods. However, the solution combustion technique has come out as cost-effective and time-saving in comparison to other methods [12]. Out of various available inorganic host matrices, we have selected $Ca_9Gd(PO_4)_7$ for doping with Sm^{3+} ions because of its high thermal and chemical stability and as far as we know, this doping is done for the first time. However, the results of the doping of Eu^{3+}, Dy^{3+}, and Eu^{2+}, Mn^{2+} ions in $Ca_9Gd(PO_4)_7$ have already been reported by Jyoti Dalal and coworkers; Lurong Yang and coworkers; Chien-Hao Huang and coworkers, respectively [21–23]. As far as we know, the structural, morphological, and luminescence properties of $Ca_9Gd(PO_4)_7$:Sm^{3+} have not been analyzed before. In this work, an attempt is made to synthesize a series of novel, orange-red-emitting, single-phase $Ca_9Gd_{(1-x)}(PO_4)_7$:xSm^{3+} ($x = 0.01 - 0.18$) nanophosphors via an economic, time-savy and efficient solution combustion method. Structural and morphological investigations are done by XRD, Rietveld, and TEM techniques. Luminescent properties of Sm^{3+}-activated $Ca_9Gd(PO_4)_7$ nanocrystalline samples are analyzed by photoluminescence excitation (PLE) spectrum, photoluminescence emission (PL) spectrum, concentration quenching, lifetime decays, etc. The optical band-gap is calculated for the best mol% system using a diffuse reflectance spectrophotometer. Further, the critical energy transfer distance (R_c) is calculated and the energy transfer mechanism being followed between different samarium ions is also discussed. The excitation wavelength 403 nm for our samples is responsible for the characteristic orange-red emission. Lastly, the results of different studies indicate that Sm^{3+}-activated $Ca_9Gd(PO_4)_7$ host is an efficient orange-red-emitting nanophosphor under near-UV excitation which might have potential utility in the field of lighting.

2 Experimental methods

2.1 Sample synthesis

The powder sample of nanophosphors having nominal composition of $Ca_9Gd_{(1-x)}(PO_4)_7$:xSm^{3+} where *x* is the dopant concentration in mol/lt varying from 0.01 to 0.18 were synthesized by solution combustion technique with following precursors: $Ca(NO_3)_2 \cdot 4H_2O$, $Gd(NO_3)_3 \cdot 6H_2O$, $Sm(NO_3)_3 \cdot 6H_2O$, $(NH_4)_2 \cdot HPO_4$, and NH_2CONH_2. All the starting materials were analytical reagent (AR) grade and used as such without undergoing any pre-treatment like purification, etc. The stoichiometric amount of the reactants and organic fuel were weighed and dissolved in a minimum amount of double-distilled water with slow stirring into a pyrex beaker to form a homogenous solution. Then, the as-obtained solution was preheated at 500 °C for few minutes in a muffle furnace that resulted in the formation of porous white voluminous powder. This step was completed via an exothermic chemical reaction that

took place inside the furnace using urea as fuel. The voluminous sample mass was then removed out of the furnace which was further cooled and crushed well in agate mortar into fine powdered form. A fraction of resultant powder was kept in an alumina crucible and transferred into the furnace where the final heating of the powder sample took place at 1200 °C for 3 h. After cooling well and grinding properly, Sm^{3+}-doped $Ca_9Gd(PO_4)_7$ nanophosphor was obtained. In the same way, sample powders of different dopant concentrations were synthesized. The chemical equation relevant to $Ca_9Gd_{0.88}Sm_{0.12}(PO_4)_7$ nanophosphor synthesis may be expressed as follows:

$$75Ca(NO_3)_2 \cdot 4H_2O + 7.333Gd(NO_3)_3 \cdot 6H_2O + Sm(NO_3)_3 \cdot 6H_2O + 58.333(NH_4)_2 \cdot HPO_4 + 875NH_2 \cdot CO \cdot NH_2 \rightarrow 8.333Ca_9Gd_{0.88}Sm_{0.12}(PO_4)_7 + 1079.167N_2 + 2362.5H_2 + 875CO_2$$

2.2 Characterization techniques

The powder X-ray diffraction (XRD) data, as-obtained from Rigaku Ultima-IV diffractometer using CuKα radiations (λ = 1.5405 Å) as a source of excitation with the operational voltage of 40 kV and 40 mA current was used to substantiate composition and phase harmony of synthesized phosphor samples. The XRD patterns were recorded in the scattering angular range (2θ) 10°–80° by maintaining a scan speed of 0.02°/s for all the samples. In Rietveld analysis, the GSAS (General Structure Analysis System) program [6, 24] was run on an X-ray diffractogram of $Ca_9Gd_{0.88}Sm_{0.12}(PO_4)_7$ phosphor for its crystal structure refinement. The morphological study of as-obtained nanophosphor was done using Technai-G^2 FEI transmission electron microscopy (TEM) maintained at a tube voltage of 200 kV. For energy band-gap evaluation in Sm^{3+}-doped $Ca_9Gd(PO_4)_7$ phosphor, Shimadzu UV-3600 plus spectrophotometer was operated from 200 to 800 nm wavelength range to obtain UV–Visible diffuse reflectance (DR) spectrum of the powdered sample. By using Hitachi F-7000 fluorescence spectrophotometer equipped with Xe lamp as the excitation source, the photoluminescence excitation (PLE) and emission (PL) spectra of all the samples were recorded at a set value of 2.5 nm for both excitation as well as emission slit width and PMT voltage taken as 400 V for higher spectral resolution. The photoluminescent decay curves were assessed on the same spectrophotometer. The chromaticity data for the complete series $Ca_9Gd_{(1-x)}(PO_4)_7{:}xSm^{3+}$ ($x = 0.01$ to 0.18) were found out with the help of MATLAB software [12]. The color coordinates of the doped phosphor were shown by the CIE1931 chromaticity plot (Standard Commission International De I'Ecleirage) [25].

All the characterization works were executed at normal room temperature and pressure conditions.

3 Results and discussion

3.1 Crystal structure refinement and phase studies

The fully indexed X-ray diffractogram for $Ca_9Gd(PO_4)_7$ and $Ca_9Gd_{(1-x)}Sm_x(PO_4)_7$ ($x = 0.01$, 0.04, 0.08, 0.10, 0.12, 0.14, 0.16, and 0.18) samples fired at 1200 °C are shown in Fig. 1. The routine procedure to check phase purity of crystalline material involves the matching of XRD profile with available JCPDS data of host matrix. However, the JCPDS data of $Ca_9Gd(PO_4)_7$ host are unavailable, but fortunately, the simulated diffraction patterns of this host are reported by Jyoti Dalal and coworkers in a recent report [21] which is shown at the bottom of Fig. 1. Now, the systematic study of various diffraction pattern of complete nanophosphor series confirms the formation of a pure crystallographic phase of the as-synthesized samples without any impurity in their crystal lattice. Hence, we can conclude that the incorporation of Sm^{3+} ion into the $Ca_9Gd(PO_4)_7$ (host) lattice does not affect its parent crystal structure of R*3c*(161) space group.

In a way to find the elaborated crystal data and to assert the purity of Sm^{3+} ion-doped $Ca_9Gd(PO_4)_7$ samples, Rietveld analysis is done using GSAS software for structural refinement at room temperature. Rietveld refinement of host material, i.e., $Ca_9Gd(PO_4)_7$ has already been reported by Jyoti Dalal and coworkers [21], whereas structural analysis of $Ca_9Gd_{0.88}Sm_{0.12}(PO_4)_7$ phosphor has been executed for the first time. Figure 2 displays the graphical Rietveld refinement result of $Ca_9Gd_{0.88}Sm_{0.12}(PO_4)_7$ sample,

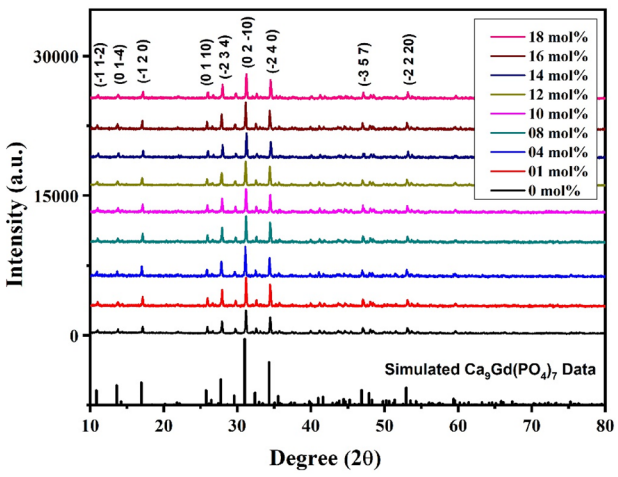

Fig. 1 Fully indexed XRD profile of $Ca_9Gd_{(1-x)}(PO_4)_7$: xSm^{3+} ($x = 0.01$ – 0.18) nanophosphors along with host-simulated $Ca_9Gd(PO_4)_7$ data

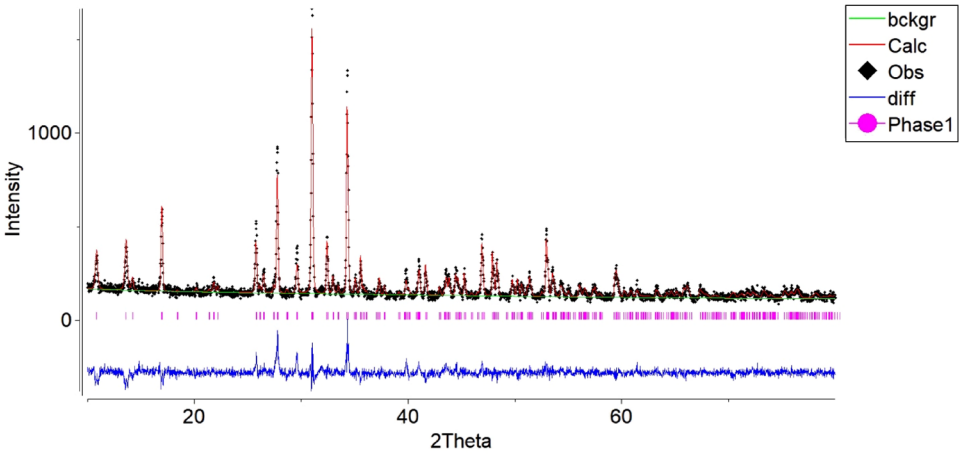

Fig. 2 Rietveld refinement of crystalline $Ca_9Gd_{0.88}Sm_{0.12}(PO_4)_7$ nanophosphor sample having parameters $\chi^2 = 1.83$, R_{wp} (%) = 10.45, and R_p (%) = 8.21

where the black triangle shows the observed diffraction pattern, however, the calculated diffraction profile is represented by a solid red line. The difference of observed and calculated diffraction pattern is given by a blue line lying just above the X-axis. The reliability parameters for $Ca_9Gd_{0.88}Sm_{0.12}(PO_4)_7$ sample come out to be $R_{wp} = 11.2\%$, $R_p = 8.5\%$, and $\chi^2 = 2.1$ indicating a good refinement of the system. This point clearly confirms the crystallization of the doped system into a pure single-phased crystal lattice. The structural analysis of $Ca_9Gd_{0.88}Sm_{0.12}(PO_4)_7$ phosphor demonstrates that this system crystallizes into trigonal lattice with R*3c*(161) space group symmetry and cell parameters $a = 10.451$ Å, $b = 10.451$ Å, $c = 37.394$ Å, $\alpha = \beta = \gamma = 90°$, $V = 3537.10$ Å^3, and $Z = 6$. The lattice parameters of our as-synthesized system is comparable with already synthesized Eu^{3+}, and Eu^{2+}, Mn^{2+} ion-doped $Ca_9Gd(PO_4)_7$ phosphors [21, 26]. Here, Table 1 summarizes the comparative study of both, host $Ca_9Gd(PO_4)_7$ and $Ca_9Gd_{0.88}Sm_{0.12}(PO_4)_7$ phosphor for different parameters relatable to crystal structure refinement. Figure 3 represents the unit cell view of $Ca_9Gd_{0.88}Sm_{0.12}(PO_4)_7$ nanophosphor inclusive of the environment surrounding of various cations. There are four kinds of crystallographic sites that have been observed in the crystal lattice of the doped phosphor for different cations like bivalent Ca^{2+} and trivalent Gd^{3+}, Sm^{3+} ions; out of which three are octa-coordinated sites shared between $Ca^{2+}/Gd^{3+}/Sm^{3+}$ ions; while the fourth site is an octahedral one for the bivalent Ca^{2+} ion [21].

However, the average crystallite size of Sm^{3+}-doped phosphor is calculated by applying Scherrer's equation on $Ca_9Gd_{0.88}Sm_{0.12}(PO_4)_7$ sample, which is as follows [6]:

$$D = \frac{0.941\lambda}{\sqrt{\left\{\beta_o^2(2\theta) - \beta_{si}^2(2\theta)\right\} \cdot Cos\theta}}, \quad (1)$$

where D is the average grain size (in nm), θ is the diffraction angle, λ be the X-ray wavelength (which is a fixed value for the instrument available, i.e., 0.1540562 nm), and $\beta_o(2\theta)$ ($\beta_{si}(2\theta)$), are the observed and standard full width at half-maximum for silicon pattern (FWHM, in radians), respectively. Working upon the above equation, the value of D is estimated to be 44.4 nm which is further confirmed by TEM pictures that are shown in Fig. 4. For $Ca_9Gd_{0.88}Sm_{0.12}(PO_4)_7$ phosphor, the TEM images show the appearance of somewhat spherical nanoparticles with agglomeration. On the basis of TEM studies, the average grain size of $Ca_9Gd_{0.88}Sm_{0.12}(PO_4)_7$ is depicted as 40–50 nm.

Kubelka and Munk gave a method to calculate the optical energy band-gap (E_g) in eV by transforming DR data values which are obtained from Shimadzu UV–Visible spectrophotometer 3600 plus. The mathematical equation describing

Table 1 The comparison of crystal structure data of $Ca_9Gd_{0.88}Sm_{0.12}(PO_4)_7$ nanophosphor system with standard $Ca_9Gd(PO_4)_7$ host lattice

Formula	$Ca_9Gd(PO_4)_7$	$Ca_9Gd_{0.88}Sm_{0.12}(PO_4)_7$
Formula weight	1182.74	1181.02
Crystal shape	Trigonal	Trigonal
Space group	R*3c*(161)	R*3c*(161)
a (Å)	10.4509(2)	10.4510(3)
b (Å)	10.4509(2)	10.4510(3)
c (Å)	37.3940(9)	37.3942(13)
$\alpha = \beta = \gamma$ (°)	90	90
Volume (Å^3)	3537.04(9)	3537.10(14)
Z	6	6
Density (g/cm^3)	3.3316	3.3234
Pearson code	hR90	hR90
Wyckoff sequence	b14a3	b14a3
R_{wp} (%)	7.49	11.24
R_p (%)	5.61	8.49
χ^2	1.05	2.11

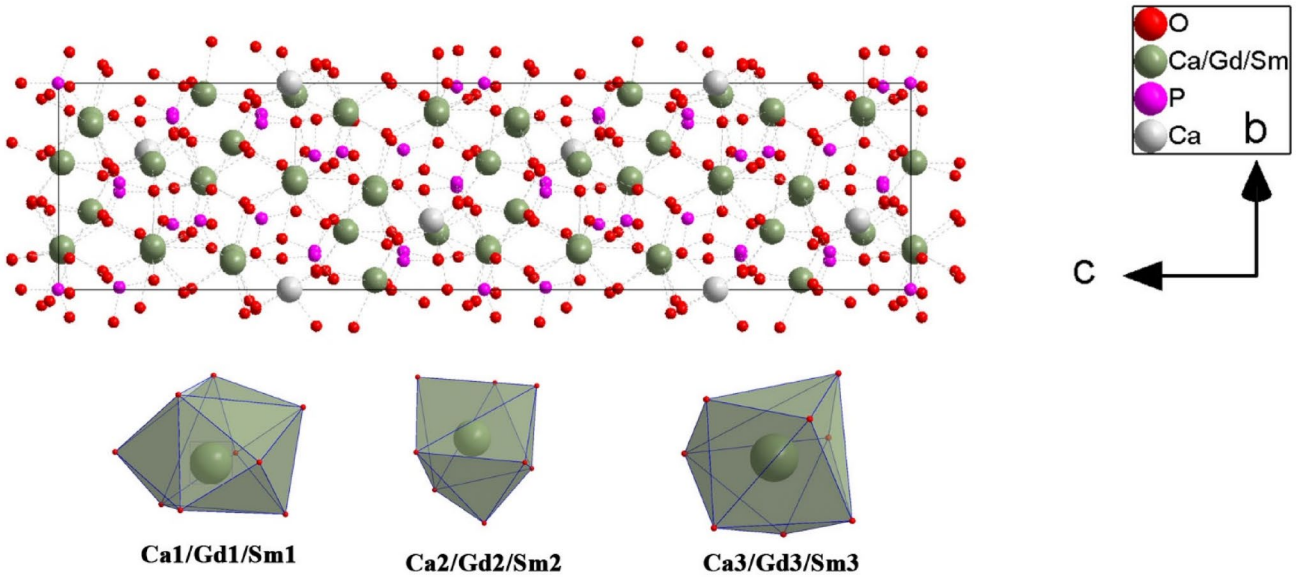

Fig. 3 Unit cell view of nanocrystals of $Ca_9Gd_{0.88}Sm_{0.12}(PO_4)_7$ along with the coordinative environment of various cations

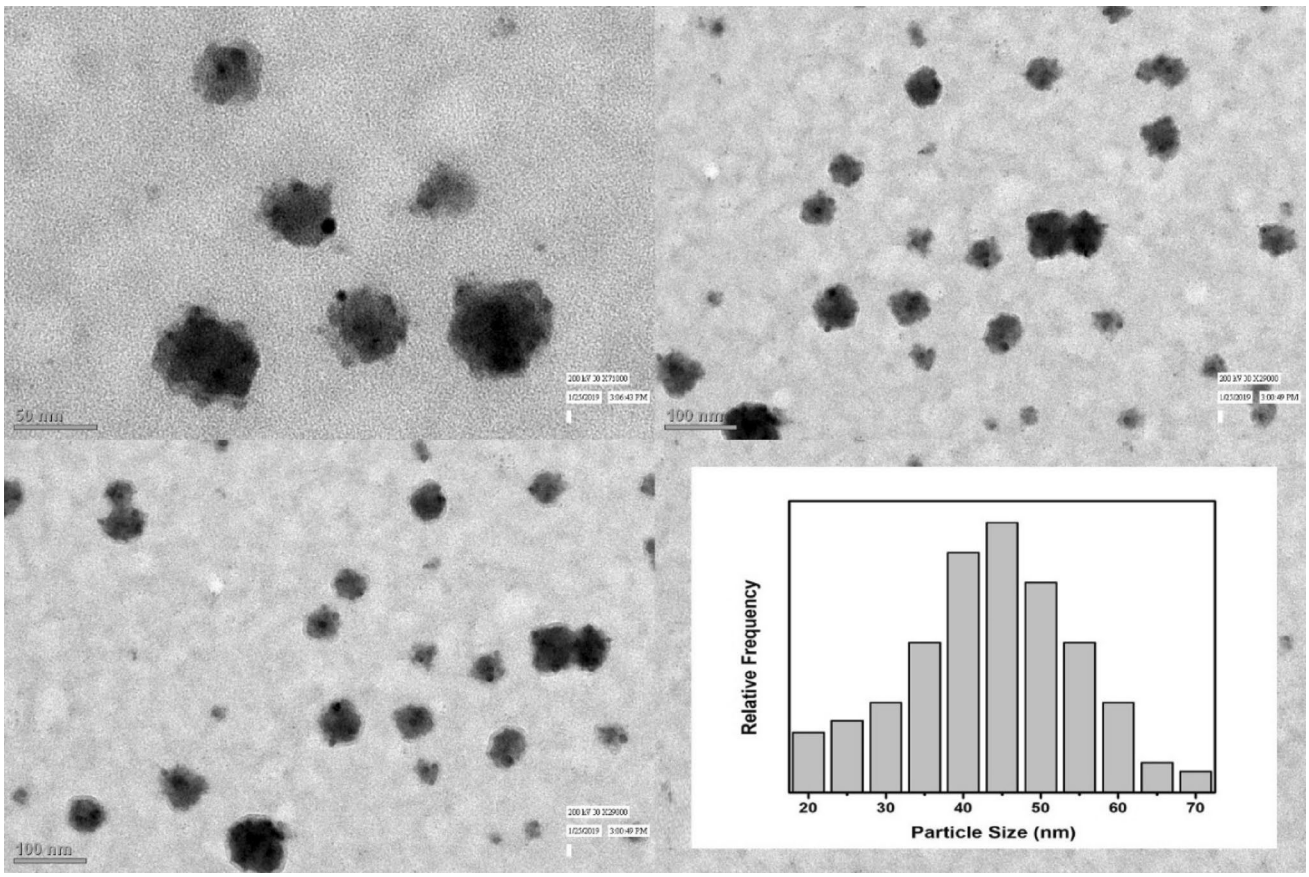

Fig. 4 TEM micrographs of $Ca_9Gd_{0.88}Sm_{0.12}(PO_4)_7$ powder calcined at 1200 °C

$F(R_\infty)$, Kubelka–Munk function $F(R_\infty)$ is written as [22, 27]

$$F(R_\infty) = \frac{(1-R_\infty)^2}{2R_\infty} = \frac{K}{S} \quad (2)$$

As per the equation cited above, K and S are the absorption and scattering coefficients, respectively; while R_∞ represents the observed reflectance of the sample. The energy absorption of all the powder samples are examined by using a general relation given below, which is also known in terms of the modified Kubelka–Munk equation [28]:

$$[F(R_\infty)h\nu]^n = C(h\nu - E_g), \quad (3)$$

where C is the proportionality constant and $h\nu$ is the energy of an incident photon. The value n depends upon the nature of electronic transitions that take place when the sample is irradiated by photons and it is 2 for a directly allowed transition and 1.5 for forbidden but direct transition, whereas values of n (0.5 and 3) are used for indirectly allowed and indirect forbidden transition, respectively. The Kubelka–Munk (K–M) plot of Sm^{3+}-doped nanophosphor of optimal concentration is obtained by applying a variation of $[F(R_\infty)h\nu]^2$ with photon energy ($h\nu$). Figure 5 represents the graphical view of the K–M plot of $Ca_9Gd_{0.88}Sm_{0.12}(PO_4)_7$ system and its diffuse reflectance spectrum is provided in the inset. From the linear extrapolation of $[F(R_\infty)h\nu]^n$ against $h\nu$ to zero, the energy band-gap (E_g) of the as-synthesized $Ca_9Gd_{0.88}Sm_{0.12}(PO_4)_7$ nanophosphor is estimated to be 4.16 eV as shown in Fig. 5; While the value of E_g for pure host $Ca_9Gd(PO_4)_7$ was reported by Jyoti Dalal et al. is 4.55 eV [21]. This notable decrease in band-gap value in the case of Sm^{3+}-doped phosphor is mainly attributed to the addition of few new electronic energy levels of the dopant ions in between the electronic states of the host. Hence, it can be resolved that $Ca_9Gd_{0.88}Sm_{0.12}(PO_4)_7$ is an appropriate nanosized phosphor for luminescent materials as it can fit new energy states created by the dopant luminescent ions within the parent energy states.

3.2 Luminescence properties

3.2.1 Luminescence spectra

The photoluminescence excitation behavior of Sm^{3+} in $Ca_9Gd(PO_4)_7$ system is analyzed by the photoluminescence excitation (PLE) spectra of 12 mol% nanophosphor ($Ca_9Gd_{0.88}Sm_{0.12}(PO_4)_7$) sample which is presented in Fig. 6. Under the emission wavelength of 600 nm, the trivalent samarium ions exhibit some characteristics luminescence peaks due to *f–f* transitions. The different characteristic peaks of trivalent samarium ion collectively yielded a brilliant orange-red emission in the visible region of EMR spectrum. The complete excitation spectrum consists of distinct excitation peaks of low and high intensity in the range 200–500 nm. The peaks located at wavelengths 344, 362, 375, 403, 417, 440, and 470 nm correspond to the electronic transitions of $^6H_{5/2} \rightarrow {}^4K_{17/2}$, $^6H_{5/2} \rightarrow {}^4H_{7/2}$, $^6H_{5/2} \rightarrow {}^6P_{7/2}$, $^6H_{5/2} \rightarrow {}^4F_{7/2}$, $^6H_{5/2} \rightarrow {}^6P_{5/2}$, $^6H_{5/2} \rightarrow {}^4G_{9/2}$, and $^6H_{5/2} \rightarrow {}^4I_{11/2}$, respectively [29]. The integrated area analysis of individual peak concludes that the peak centered at 403 nm is the most intense peak in comparison with the other excitation peaks which is assigned to $^6H_{5/2} \rightarrow {}^4F_{7/2}$ transition.

Figure 7 represents the photoluminescence emission (PL) spectra (at $\lambda_{ex} = 403$ nm) of Sm^{3+}-activated $Ca_9Gd(PO_4)_7$

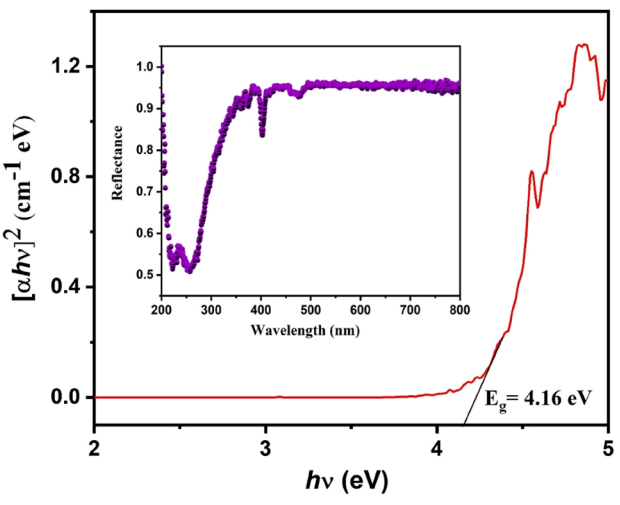

Fig. 5 The relationship between the absorption coefficient and phonon energy for $Ca_9Gd_{0.88}Sm_{0.12}(PO_4)_7$ nanophosphor with inset displaying its corresponding DR spectra

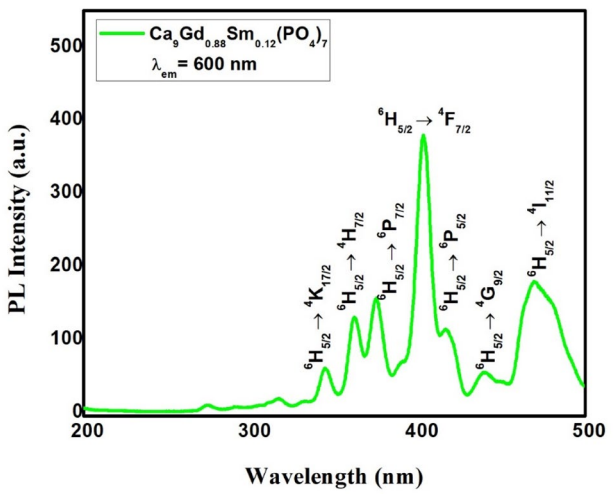

Fig. 6 PL Excitation spectrum of $Ca_9Gd_{(1-x)}Sm_x(PO_4)_7$ ($x = 0.12$) nanophosphor studied at $\lambda_{em} = 600$ nm

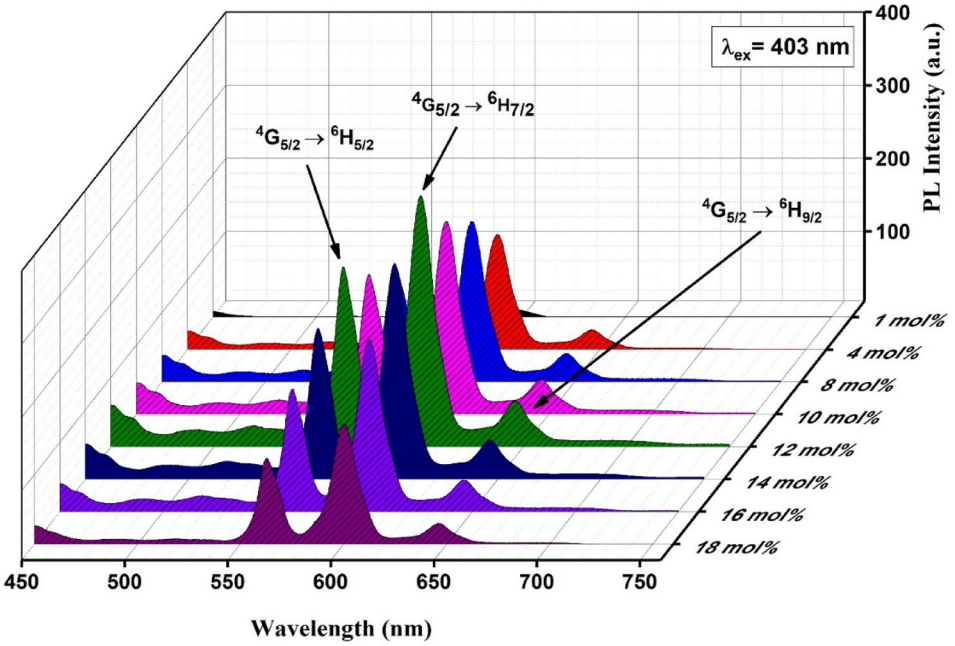

Fig. 7 PL emission spectra of $Ca_9Gd_{(1-x)}Sm_x(PO_4)_7$ ($x = 0.01$–0.18) nanophosphors studied at $\lambda_{ex} = 403$ nm

nanophosphor system at different concentrations of activator ions. A comprehensive analysis of PL emission spectral lines of all the mol% samples shows that different emission patterns are identical in their peak position and shape but they differ in the relative intensities of various peaks. In the emission spectra of $Ca_9Gd_{(1-x)}Sm_x(PO_4)_7$ ($x = 0.01$, 0.04, 0.08, 0.10, 0.12, 0.14, 0.16, and 0.18) nanocrystalline systems the characteristic emission bands of Sm^{3+} ions are observed at wavelengths 563, 600, and 646 nm which are associated with $^4G_{5/2} \rightarrow {}^6H_{5/2}$, $^4G_{5/2} \rightarrow {}^6H_{7/2}$, and $^4G_{5/2} \rightarrow {}^6H_{9/2}$ transitions, respectively [30, 31]. From integrated area analysis of emission spectra, it has been observed that the emission peak at 600 nm ($^4G_{5/2} \rightarrow {}^6H_{7/2}$) is the strongest one. As per selection rule ($\Delta J = \pm 1$), the peak corresponding to $^4G_{5/2} \rightarrow {}^6H_{5/2}$ (563 nm) is purely magnetic dipole transition while $^4G_{5/2} \rightarrow {}^6H_{7/2}$ (600 nm) is partially magnetic and partially electric dipole transition and the third peak at 646 nm ($^4G_{5/2} \rightarrow {}^6H_{9/2}$) is purely electric dipole transition [4, 18]. From Fig. 7, it can be seen that with an increase in the concentration of Sm^{3+} ions, PL intensity increases, reaches a maximum at 12 mol%, and then decreases gradually beyond this critical concentration. This downfall may be attributed to the increase in the non-radiative transitions at higher concentrations of Sm^{3+} ions. For a resolved analysis, PL excitation and emission spectra of the best mol% concentration of dopant ion over an entire range of wavelength 200–800 nm are shown in Fig. 8. Lastly, it can be easily depicted from PL spectral analysis that $Ca_9Gd_{0.88}(PO_4)_7$:$0.12Sm^{3+}$ nanophosphor has applicability to be used as near-UV-excited phosphor because it shows maximum PL emission intensity under excitation at 403 nm.

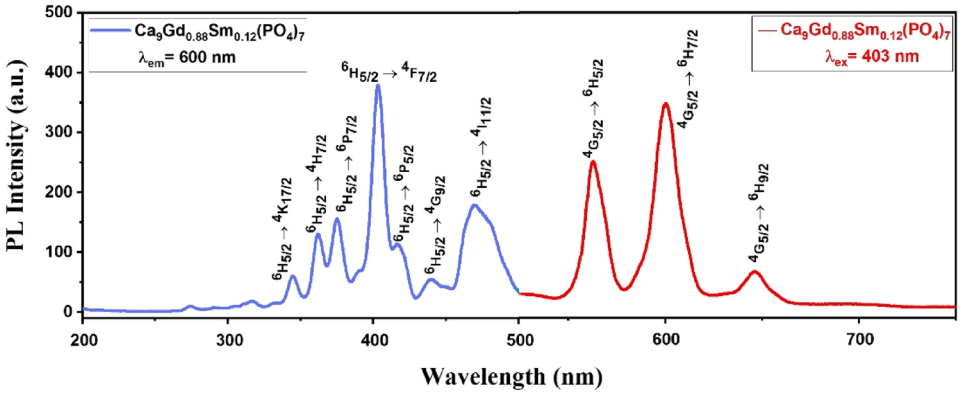

Fig. 8 A combined PL Excitation ($\lambda_{em} = 600$ nm) and PL emission ($\lambda_{ex} = 403$ nm) spectra of $Ca_9Gd_{0.88}Sm_{0.12}(PO_4)_7$) nanocrystalline system

3.2.2 Energy transfer mechanism

To interpret the luminescence properties of Sm^{3+}-activated $Ca_9Gd(PO_4)_7$ in a finer way, a schematic electronic energy-level diagram showing all the feasible transitions among various energy states of Sm^{3+} ion is shown in Fig. 9. As per the above-mentioned diagram, firstly Sm^{3+} ions are excited from $^6H_{5/2}$ to different high-energy states like $^4F_{7/2}$ (most populated), $^4K_{17/2}$, $^4H_{7/2}$, $^6P_{7/2}$, $^6P_{5/2}$, $^4G_{9/2}$, and $^4I_{11/2}$ levels which are quickly followed by the non-radiative relaxation to the $^4G_{5/2}$ low-lying emitting state. Then, radiative transitions occur from $^4G_{5/2}$ to ^6H_J ($J = 5/2$, 7/2, 9/2), and the cumulative influence of these emission transition results in characteristic orange-red color of Sm^{3+} ions. Now, Fig. 10 is displaying the effect of concentration of Sm^{3+} ions on the photoluminescence emission intensities as observed at 600 nm emission wavelength. It is determined from this plot that emission intensity increases initially until 12 mol% (known as critical concentration), and then decreases with further increase in the concentration of trivalent samarium ion. The reduction of the PL intensities may be attributed to the occurrence of non-radiative energy transfer due to the well-established concentration quenching effect [22, 32]. The phenomenon of concentration quenching can be explained by a fact that with the increase in the concentration, the distance between activator ions is decreased due to which probability of non-radiative energy transfer among Sm^{3+} ions becomes higher. This behavior of non-radiative energy transfer mainly arises from energy re-absorption, exchange interaction, and electric multipole–multipole interactions [33]. According to the report of Blasse, at optimum concentration, the distance between adjacent Sm^{3+} ions can be calculated which is

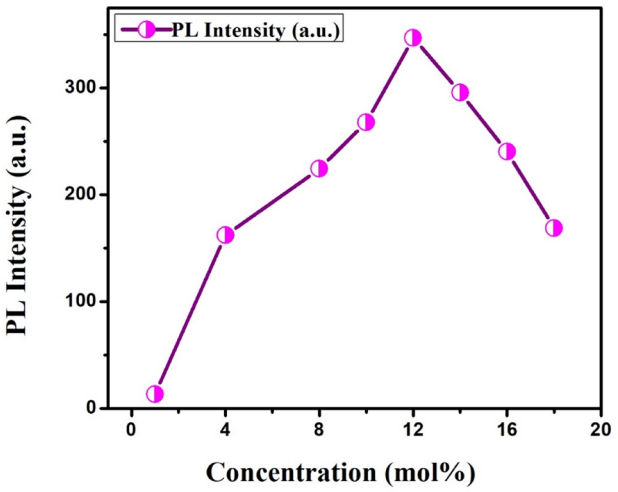

Fig. 10 Variation of the emission intensity as a function of Sm^{3+} concentration in $Ca_9Gd_{(1-x)}(PO_4)_7$: xSm^{3+}($x = 0.01$–0.18) nanophosphors

known as critical energy transfer distance (R_c) and this value of R_c is quite helpful in proposing the mechanism responsible for non-radiative energy transfer [33–35]. The value of R_c for $Ca_9Gd_{0.88}Sm_{0.12}(PO_4)_7$ nanophosphor is calculated by using the equation as follows [4, 32, 36]:

$$R_c = 2\left[\frac{3V}{4\pi x_c N}\right]^{1/3}. \quad (4)$$

where V represents the volume of a unit cell, x_c is an optimum concentration of activator ions, and N is the number of cations which are replaced by Sm^{3+} ions in a crystallographic unit. Now, putting $V = 3537.10$ Å^3, $N = 6$, and $x_c = 0.12$ into

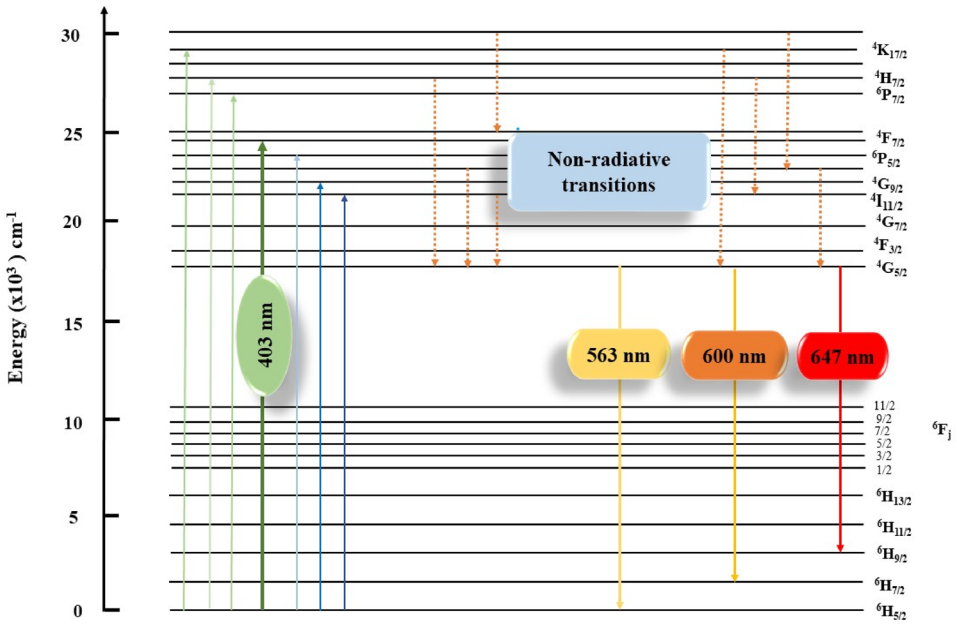

Fig. 9 Energy transfer mechanism in Sm^{3+} ions for $Ca_9Gd(PO_4)_7$:Sm^{3+} nanophosphors

the Blasse equation, value of R_c obtained is about 21 Å. The value of R_c is much higher than 5 Å, which is a limiting value of critical distance for exchange interaction. So, the possibility of energy transfer via exchange interaction is eliminated, and also the possibility of energy re-absorption is ruled out here because no overlapping of PL excitation and emission spectra is observed. The only presumptive mechanism type left behind for energy transfer between luminescent centers in $Ca_9Gd_{0.88}Sm_{0.12}(PO_4)_7$ according to Dexter's theory is electric multipolar interaction which is categorized into electric dipole–dipole (d–d), dipole–quadrupole (d–q), and quadrupole–quadrupole (q–q) interactions [4, 6, 37–39].

Huang et al. also developed the correlation between the photoluminescence emission intensity and the doping concentration after best-emission concentration as [40, 41]

$$log\left(\frac{I}{x}\right) = log(f) - \left(\frac{Q}{3}\right)logx, \tag{5}$$

where x be the activator ion (Sm^{3+}) concentration, I is the integral intensity of emission spectra, I/x is emission intensity per activator ion, f is a concentration-independent constant, Q is a measure of electric multipolar interaction, as the values of $Q = 6$, 8, or 10 represent dipole–dipole (d–d), dipole–quadrupole (d–q), or quadrupole–quadrupole (q–q) interactions, respectively. Using the above equation, a straight-line plot of the log I/x versus log x is obtained with a negative slope and the corresponding fitted line is shown in Fig. 11. From this plot, we get the value of slope as − 2.62, which correlates with the value of – (Q/3) in the above-mentioned equation of straight line. All this concludes the value of $Q = 7.86$ for $Ca_9Gd_{0.88}(PO_4)_7$:$0.12Sm^{3+}$ nanophosphor which is close to the theoretical value 8. Hence, the type of non-radiative energy transfer mechanism most likely to be favored in $Ca_9Gd_{(1-x)}Sm_x(PO_4)_7$ ($x = 0.01$–0.18) nanophosphors is electric dipole–quadrupole interactions.

3.2.3 Lifetime decay

The lifetime decay profile of $Ca_9Gd_{(1-x)}Sm_x(PO_4)_7$ nanophosphors for various concentrations ($x = 0.01$ to 0.18) of dopant ion is studied at an excitation wavelength of 403 nm and an emission wavelength of 600 nm. Figure 12 clearly shows that the photoluminescence lifetime decreases with an increase in Sm^{3+} ion concentration reason being that the probability of non-radiative relaxation gets increased with concentration. The nature of the decay curve is exponential and as-obtained lifetime values (ms) follow the triple-exponential fitting parameters, well that can be shown by the following equation [42]:

$$I(t) = I_0 + A_1 exp\left(\frac{-t}{\tau_1}\right) + A_2 exp\left(\frac{-t}{\tau_2}\right) + A_3 exp\left(\frac{-t}{\tau_3}\right) \tag{6}$$

where $I(t)$ is the photoluminescence intensity at time t; I_0 is the PL intensity at time 0; A_1, A_2, and A_3 are the intensity constants and τ_1, τ_2, and τ_3 are the total (radiative and non-radiative) time for the exponential decay. The triple-exponential fit nature of decay curves further speculates the presence of three different types of sites in $Ca_9Gd(PO_4)_7$ lattice for Sm^{3+} ions. The average or effective decay lifetime (τ_{avg}) is calculated using the equation which is as follows [42]:

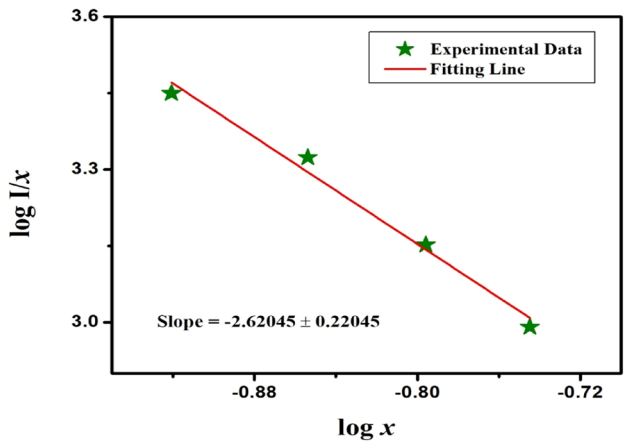

Fig. 11 Plot of log(I/x) as a function of log(x) in $Ca_9Gd(PO_4)_7$:Sm^{3+} nanophosphors

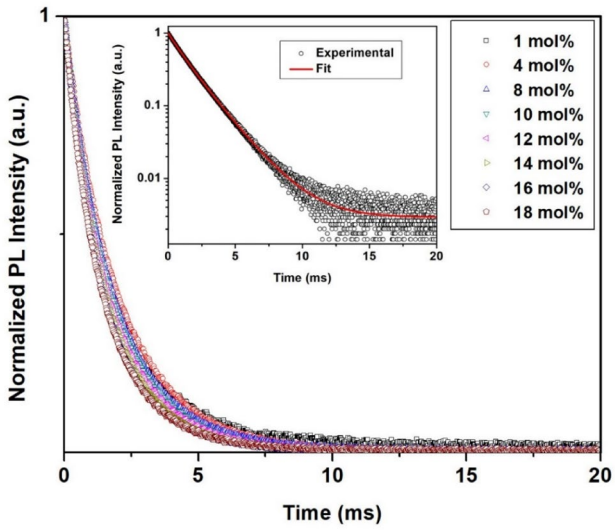

Fig. 12 The luminescence decay curves for the emission of $Ca_9Gd_{(1-x)}Sm_x(PO_4)_7$ ($x = 0.01$–0.18) nanocrystals

Table 2 Photoluminescence lifetime, non-radiative rates, and quantum efficiencies of $^4G_{5/2}$ state in $Ca_9Gd_{(1-x)}Sm_x(PO_4)_7$ ($x = 0.01$–0.18) nanophosphors

S. no	Sm^{3+} concentrations (mol%)	Average lifetime (ms)	Non-radiative rates (s^{-1})	Quantum efficiency (%)
1	1	2.301	17.9	95.8
2	4	2.232	31.4	93.0
3	8	1.925	102.8	80.2
4	10	1.868	118.7	77.8
5	12	1.787	142.9	74.5
6	14	1.703	170.5	70.9
7	16	1.634	195.3	68.1
8	18	1.608	205.1	67.0

$$\tau_{avg} = \frac{(A_1\tau_1^2 + A_2\tau_2^2 + A_3\tau_3^2)}{(A_1\tau_1 + A_2\tau_2 + A_3\tau_3)} \tag{7}$$

The values of observed lifetime come out to be 2.30, 2.23, 1.92, 1.86, 1.78, 1.70, 1.63, and 1.60 ms for 1, 4, 8, 10, 12, 14, 16, and 18 mol% Sm^{3+} ion concentrations, respectively, and these values (ms) for the complete series of $Ca_9Gd_{(1-x)}(PO_4)_7$:xSm^{3+} nanophosphors are listed in Table 2.

To analyze this gradational downfall in decay time with the concentration of Sm^{3+} ions, Auzel's fitting function is employed on these lifetime values to get intrinsic lifetime data for $Ca_9Gd_{(1-x)}(PO_4)_7$:xSm^{3+} nanophosphors. The distinguished expression for the same fitting is written as [40, 43, 44]

$$\tau(c) = \frac{\tau_R}{1 + \left(\frac{c}{c_0}\right)e^{-N/3}} \tag{8}$$

As per the equation cited above, $\tau(c)$ is the total lifetime (radiative + non-radiative) value at concentration c, τ_R be the intrinsic radiative lifetime for the emitting state, c and c_o are the constants for a concentration, N represents the number of phonons generated from the emitting state. For $^4G_{5/2}$ state, intrinsic radiative lifetime (τ_R) is calculated as 2.40 ms and numbers of phonons generated out to be 11.34 which is ~ 11. The Auzel's fitting curve along with all the important information is displayed in Fig. 13.

Once the intrinsic lifetime (τ_R) value is known, the quantum efficiencies (ϕ) of $^4G_{5/2}$ state for a series of $Ca_9Gd_{(1-x)}(PO_4)_7$:xSm^{3+} ($x = 0.01$ to 0.18) nanocrystalline phosphors can be ascertained by using the following mathematical expression [21, 45–47]:

$$\phi = \frac{\tau_o}{\tau_R} = \frac{A_R}{A_R + A_{nR}} \tag{9}$$

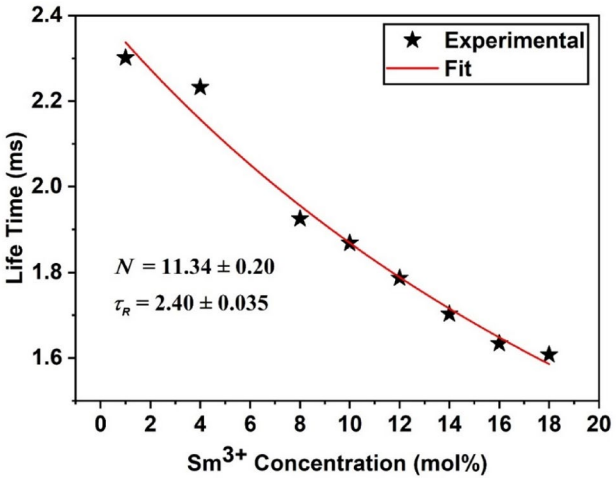

Fig. 13 Dependence of photoluminescence lifetime of $^4G_{5/2}$ level on the doping concentration of Sm^{3+} ion using Auzel's modal

Here, τ_o and τ_R represent the observed and intrinsic lifetime, respectively; while A_R and A_{nR} are radiative and non-radiative rates of relaxation, respectively. By modifying the above-mentioned equation, non-radiative rates (s^{-1}) can be calculated by using the equation given as

$$\frac{1}{\tau_o} - \frac{1}{\tau_R} = A_{nR} \tag{10}$$

All the as-obtained results for quantum efficiencies and non-radiative rates for the whole series of Sm^{3+}-doped $Ca_9Gd(PO_4)_7$ nanophosphors are collected in Table 2, and it is suggested that nanophosphor $Ca_9Gd_{0.88}Sm_{0.12}(PO_4)_7$ with considerably good quantum efficiency (~ 75%) has potential applications in the field of lighting and display.

3.2.4 CIE chromaticity diagram

To further analyze one of the very interesting luminescence property, i.e., emission color, the chromaticity coordinates for the whole series of $Ca_9Gd_{(1-x)}Sm_x(PO_4)_7$ ($x = 0.01$–0.18) nanophosphors at $\lambda_{ex} = 403$ nm are calculated using the MATLAB software program and are represented in Table 3. Figure 14 displays the CIE chromaticity diagram [48, 49] for the critical concentration of the system whose color coordinates are labeled by a black dot symbol. For $Ca_9Gd_{0.88}Sm_{0.12}(PO_4)_7$ nanophosphor, chromaticity coordinates are found to be $x = 0.5113$ and $y = 0.4628$, respectively. The color coordinate values confirm the emission of synthesized phosphors in the orange-red region of the visible spectrum indicating potential applications in display and lighting. Furthermore, such nanocrystalline phosphors with high quantum efficiencies can be used to develop near-UV-based WLEDs.

Table 3 CIE1931 chromaticity index for $Ca_9Gd_{(1-x)}Sm_x(PO_4)_7$ ($x = 0.01$–0.18) nanophosphors

S. no	Sm^{3+} concentrations (mol%)	CIE color coordinates (x, y)
1	1	(0.4564, 0.4949)
2	4	(0.5125, 0.4567)
3	8	(0.5105, 0.4630)
4	10	(0.5126, 0.4625)
5	12	(0.5113, 0.4628)
6	14	(0.5106, 0.4632)
7	16	(0.5063, 0.4650)
8	18	(0.5174, 0.4593)

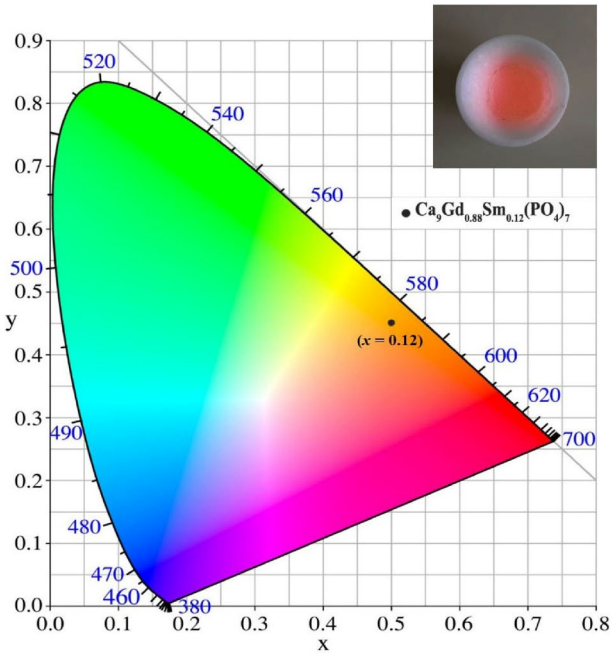

Fig. 14 CIE1931 chromaticity diagram for $Ca_9Gd_{(1-x)}Sm_x(PO_4)_7$ ($x = 0.12$) nanophosphor

4 Conclusion

A series of the novel, Sm^{3+}-doped, orange-red-emitting $Ca_9Gd(PO_4)_7$ nanophosphors were synthesized using a competent solution combustion method at 1200 °C. Their structural, morphological, and photoluminescence properties were investigated by the help of XRD, Rietveld, PL, and TEM analyses. Rietveld refinement of $Ca_9Gd_{0.88}Sm_{0.12}(PO_4)_7$ system confirmed the trigonal structure of nanocrystal with R*3c*(161) space group. The average crystallite size was calculated in the range of 40–50 nm which was further confirmed by TEM micrographs. The energy band-gap value for xSm^{3+}-doped $Ca_9Gd(PO_4)_7$ nanophosphor ($x = 12$ mol%) was found to be 4.16 eV by examining diffuse reflectance data. Critical distance (R_c) between adjacent Sm^{3+} ions was calculated to be 21 Å. The energy-level diagram describes all the radiative transitions and phenomenon of non-radiative relaxation occurring between different electronic energy levels of Sm^{3+} ions. PL emission spectra revealed the presence of various peaks at 563, 600, and 646 nm corresponding to the $^4G_{5/2} \rightarrow {}^6H_{5/2}$, $^4G_{5/2} \rightarrow {}^6H_{7/2}$, and $^4G_{5/2} \rightarrow {}^6H_{9/2}$ transitions, respectively. The decay profile and average lifetime for different concentrations of Sm^{3+} were analyzed in detail. The Auzel's fitting modal was applied to calculate intrinsic radiative lifetime (2.40 ms), non-radiative rate 142.9 s^{-1}, and quantum efficiency (74.5%) for the $Ca_9Gd(PO_4)_7$:$0.12Sm^{3+}$ system. The color coordinates for $Ca_9Gd_{0.88}Sm_{0.12}(PO_4)_7$ nanophosphor were obtained as (0.5113, 0.4628). All the structural and luminescence results suggest that Sm^{3+}-doped $Ca_9Gd(PO_4)_7$ nanophosphors are appropriate candidate for near-UV excitation and thus, have a bright domain in WLEDs.

References

1. L. Sun, B. Devakumar, B. Li, J. Liang, H. Guo, X. Huang, RSC Adv. **8**, 23284–23293 (2018)
2. H. Guo, L. Sun, J. Liang, B. Li, X. Huang, J. Lumin. **205**, 115–121 (2019)
3. H. Xu, L. Wang, D. Qu, Z. Si, J. Shi, RSC Adv. **7**, 41282–41288 (2017)
4. B. Ma, X. Ma, T. Xu, K. Su, Q. Zhang, RSC Adv. **8**, 14164–14170 (2018)
5. M.M. Kimani, J.W. Kolis, J. Lumin. **145**, 492–497 (2014)
6. H. Dahiya, M. Dalal, J. Dalal, V.B. Taxak, S.P. Khatkar, D. Kumar, Mater. Res. **99**, 86–92 (2018)
7. M. Dalal, V.B. Taxak, J. Dalal, A. Khatkar, S. Chahar, R. Devi, S.P. Khatkar, J. Alloys Compd. **698**, 662–672 (2017)
8. G.G. Wang, X.F. Wang, L.W. Dong, Q. Yang, RSC Adv. **6**, 42770–42777 (2016)
9. M. Dalal, V.B. Taxak, S. Chahar, J. Dalal, A. Khatkar, S.P. Khatkar, J. Alloys Compd. **686**, 366–374 (2016)
10. S. Chahar, V.B. Taxak, M. Dalal, S. Singh, S.P. Khatkar, Mater. Res. **77**, 91–100 (2016)
11. H. Dahiya, M. Dalal, A. Siwach, J. Dalal, V.B. Taxak, S.P. Khatkar, D. Kumar, J. Mater. Sci. (2019). https://doi.org/10.1007/s10854-019-02009-1
12. H. Dahiya, M. Dalal, A. Siwach, M. Dahiya, D. Kumar, J. Mater. Sci. **29**, 20750–20758 (2018)
13. E. Pavitra, G.S. Raju, Y.H. Ko, J.S. Yu, Phys. Chem. Chem. Phys. **14**, 11296–11307 (2012)
14. G. Zhu, Z. Ci, Y. Shi, M. Que, Q. Wang, Y. Wang, J. Mater. Chem. **1**, 5960–5969 (2013)
15. Y. Wang, X. Liu, Y. Li, L. Jing, J. Alloys Compd. **653**, 315–320 (2015)
16. X. Zhang, L. Zhou, M. Gong, Opt. Mater. **35**, 993–997 (2013)
17. Z. Yang, H. Dong, P. Liu, C. Hou, X. Liang, C. Wang, F. Lu, J. Rare Earths **32**, 404–408 (2014)
18. R. Nagaraja, V. Pushpa Manjari, B. Sailaja, R.V.S.S.N. Ravikumar, J. Mol. Struct. **1130**, 96–102 (2017)

19. H. Xia, J. Feng, Y. Ji, J. Xu, Z. Zhu, Y. Wang, Z. You, J. Li, H. Wang, C. Tu, J. Lumin. **149**, 7–11 (2014)
20. M. Dalal, V.B. Taxak, S. Chahar, A. Khatkar, S.P. Khatkar, J. Phys. Chem. Solids **89**, 45–52 (2016)
21. J. Dalal, M. Dalal, S. Devi, R. Devi, A. Hooda, A. Khatkar, V.B. Taxak, S.P. Khatkar, J. Lumin. **210**, 293–302 (2019)
22. L. Yang, Z. Mu, S. Zhang, Q. Wang, D. Zhu, Y. Zhao, D. Luo, Q. Zhang, F. Wu, J. Mater. Sci. **29**, 6548–6555 (2018)
23. C.H. Huang, W.-R. Liu, T.-M. Chen, J. Phys. Chem. **114**, 18698–18701 (2010)
24. J. Dalal, M. Dalal, S. Devi, S. Chahar, A. Hooda, A. Khatkar, R.K. Malik, V.B. Taxak, S.P. Khatkar, Methods Appl. Fluoresc. (2019). https://doi.org/10.1088/2050-6120/ab33b6
25. S. Chahar, R. Devi, M. Dalal, M. Bala, J. Dalal, P. Boora, V.B. Taxak, R. Lather, S.P. Khatkar, Ceram. Int. **45**, 606–613 (2019)
26. N. Guo, H. You, Y. Song, M. Yang, K. Liu, Y. Zheng, Y. Huang, H. Zhang, J. Mater. Chem. (2010). https://doi.org/10.1039/c0jm01860k
27. J. Zhao, C. Guo, T. Li, D. Song, X. Su, Phys. Chem. Chem. Phys. **17**, 26330–26337 (2015)
28. L. Wang, H.M. Noh, B.K. Moon, S.H. Park, K.H. Kim, J. Shi, J.H. Jeong, J. Phys. Chem. **119**, 15517–15525 (2015)
29. Z. Yang, D. Xu, J. Sun, Y. Sun, H. Du, Opt. Eng. **54**(10), 105102 (2015)
30. Y. Shi, J. Shi, C. Dong, Ceram. Int. **43**, 16356–16361 (2017)
31. V. Kumar, A.K. Bedyal, S.S. Pitale, O.M. Ntwaeaborwa, H.C. Swart, J. Alloys Compd. **554**, 214–220 (2013)
32. R. Yu, H.M. Noh, B.K. Moon, B.C. Choi, J.H. Jeong, H.S. Lee, K. Jang, S.S. Yi, J. Lumin. **152**, 133–137 (2014)
33. X. Zhang, L. Zhou, Q. Pang, M. Gong, RSC Adv. **5**, 54622–54628 (2015)
34. Q. Sun, B. Li, S. Wang, H. Guo, X. Huang, J. Mater. Sci. **29**, 12972–12977 (2018)
35. Z. Yang, P. Liu, J. Li, Q. Yang, L. Lv, Y. Zhao, J. Alloys Compd. **578**, 118–120 (2013)
36. A.K. Bedyal, V. Kumar, O.M. Ntwaeaborwa, H.C. Swart, Mater. Res. **1**, 015006–015012 (2014)
37. L. Sun, H. Guo, J. Liang, B. Li, X. Huang, J. Lumin. **202**, 403–408 (2018)
38. C.H. Huang, Y.T. Lai, T.S. Chan, Y.T. Yeh, W.R. Liu, RSC Adv. **4**, 7811–7817 (2014)
39. M. Jiao, Y. Jia, W. Lü, W. Lv, Q. Zhao, B. Shao, H. You, J. Mater. Chem. C **2**, 90–97 (2014)
40. X. Huang, Opt. Mater. **50**, 81–86 (2015)
41. Y. Tian, B. Chen, B. Tian, R. Hua, J. Sun, L. Cheng, H. Zhong, X. Li, J. Zhang, Y. Zheng, T. Yu, L. Huang, Q. Meng, J. Alloys Compd. **509**, 6096–6101 (2011)
42. Z.W. Zhang, L. Liu, R. Liu, X.Y. Zhang, X.G. Peng, C.H. Wang, D.J. Wang, Materials **167**, 250–253 (2016)
43. Y. Tian, B. Chen, R. Hua, J. Sun, L. Cheng, H. Zhong, X. Li, J. Zhang, Y. Zheng, T. Yu, L. Huang, H. Yu, J. Appl. Phys. **109**, 053511–053516 (2011)
44. Z. Liu, Q. Meng, H. Liu, C. Yao, Q. Meng, W. Liu, W. Wang, Opt. Mater. **36**, 384–389 (2013)
45. R. Devi, M. Dalal, M. Bala, S.P. Khatkar, V.B. Taxak, P. Boora, J. Mater. Sci. **27**, 12506–12516 (2016)
46. M. Ferhi, C. Bouzidi, K. Horchani-Naifer, H. Elhouichet, M. Ferid, Opt. Mater. **37**, 607–613 (2014)
47. S.H. Bindu, T.R. Rao, C.L. Raju, Phys. Scr. **90**, 065802 (2015)
48. Z. Zhou, N. Wang, N. Zhou, Z. He, S. Liu, Y. Liu, Z. Tian, Z. Mao, H.T. Hintzen, J. Phys. D **46**, 035104 (2013)
49. D. Wu, W. Xiao, L. Zhang, X. Zhang, Z. Hao, G.-H. Pan, Y. Luo, J. Zhang, J. Mater. Chem. **5**, 11910–11919 (2017)